Combined microgravity, electrical resistivity tomography and induced polarization to detect deeply buried caves: Algaidilla cave (Southern Spain)

Martínez-Moreno, F.J.[1], Pedrera, A.[2], Ruano, P.[1,2], Galindo-Zaldívar, J.[1,2], Martos-Rosillo, S.[3],
González-Castillo, L.[1], Sánchez-Úbeda, J.P.[1], and Marín-Lechado C.[3]

[1] Departamento de Geodinámica, Universidad de Granada, 18071-Granada, Spain (franmartinez@ugr.es; jgalindo@ugr.es; pruano@ugr.es)

[2] Instituto Andaluz de Ciencias de la Tierra, CSIC-Universidad de Granada, 18071-Granada, Spain (mailto:pedrera@ugr.es)

[3] Instituto Geológico y Minero de España- Ríos Rosas 23, 28003 Madrid, Spain (s.martos@igme.es; c.marin@igme.es)

Abstract

The suitability of the combined microgravity and electrical tomography to detect and characterize caves deeply buried in limestones is tested. We have selected the buried Algaidilla cave, in the Estepa range (western Betic Cordillera), which is partially submerged below the water table and which was intersected between 26 and 66 m in depth by two boreholes. At that location, microgravity, electrical resistivity tomography (ERT) and induced polarization (IP) data was collected along four profiles. Algaidilla cave is associated with a -0.5 mGal residual gravity anomaly minimum. Microgravity models reveal an approximately horizontal N-S elongated shape with a maximum length of 150 m and a width of 40 m. Resistivity variations provide information on the cave sectors remaining above, as well as below the water table. Forward modeling and depth of investigation (DOI) support the suitability of ERT to constrain the cave geometry. The cave is identified as having an intermediate to low-resistivity feature, which approximately matches the 250 ohm·m contour line along its ceiling. In addition, induced polarization models show high chargeability anomalies probably associated with decalcification clays. The location and approximately geometry of Algaidilla cave estimated from geophysical modeling suggests that nearby overburden may develop cave-ins and collapse sinkholes. Microgravity is proved as a powerful tool to detect caves at this depth, but this method alone fails to estimate the geometry. ERT results delineate the cavity both above and below the water table. Although the deepest sectors of the models should be interpreted with caution since they are less constrained by the data, below the water table the cavity shows great resistivity contrast with regard to the background carbonate. In addition, this study points out the usefulness of the IP method for detecting decalcification clays, often present at the base of karstic caves.

Keywords: Microgravity, electrical resistivity tomography, induced polarization, deep-cave geometry, DOI index, forward modeling.

1. Introduction

The study of karst cavities is of great interest in the fields of civil engineering and hydrogeology. Firstly, subsidence by the collapse of karst cavities can have particular impacts on transport infrastructure and building. Secondly, karst cavities determine the hydrodynamics of carbonate aquifers, which constitute an important water resource in arid and semiarid regions, since these aquifers have a high rate of recharge, large storage capacity, and good water quality. Some karstic cavities are accessible from the surface and their size allows direct description and mapping. However, many caves remain disconnected from the surface or are connected by narrow fissures. These cavities must be characterized indirectly by geophysical methods.

Gravity methods have been used to detect near-surface caves since the 1960s (Chico, 1964; Butler, 1984), and electrical prospecting has been used since the 1980s (Smith and Randazzo, 1975; Owen, 1983; Chamon and Dobereiner, 1988; Rodríguez and Reyes, 1992). In recent years, electrical resistivity tomography (ERT) has developed as a key technique to image near-surface geological structures, including cave detection (McGrath et al., 2002; Zhou et al., 2004; El Qady et al., 2005; Carpenter and Ekberg, 2006; Leucci and Giorgi, 2005; Leucci, 2006; Rădulescu et al., 2007; Vargemezis et al., 2007; Abu-Shariah, 2009; Ravbar and Kovačič, 2010; Cardarelli et al., 2010; Lazzari et al., 2010; Ortega et al., 2010; Pánek et al, 2010; Valois et al., 2010; Gambetta et al., 2011). Numerous combinations of gravity and electrical methods with other geophysical techniques have been used to detect superficial caves (Table 1). However, rarely these combinations of techniques reaches a depth greater than 40 m. Focusing on the combined microgravity and ERT methods, McGrath et al. (2002) successfully documented karstic voids up to 5 m deep. Recently, Gambetta et al. (2011)

satisfactorily tested the gravity and electrical response of a known shallow cave segment located at, or about, 30 m from the ground surface.

The aim of the present study is to test the suitability of combining microgravity, ERT and IP in order to detect and characterize karstic caves buried more than 30 m below the ground surface. We selected a buried cave located in the Estepa range (western Betic Cordillera), intersected by two boreholes between 26 and 66 m depth, in order to characterize its geometry combining these geophysical techniques.

2. Geological and hydrogeological setting

The Betic Cordillera is the westernmost end of the European Alpine Chain and, together with the Rif, forms the Gibraltar Tectonic Arc. Three major geological zones are recognized in the Betic Cordillera: the Internal Zones, the Campo de Gibraltar Flysch Complex, and the External Zones. The External Zones are composed mainly of Mesozoic limestones that extensively crop out WSW-ENE along the north-western border of the Betic Cordillera (Fig. 1a). These are divided into the Prebetic and Subbetic sedimentary sequences deposited close and far, respectively from the South Iberian palaeomargin (García-Hernández, 1980). These rocks are deformed by folds and thrusts with a general vergence towards the NW (Fig. 1b). In the western part of the Betic Cordillera, the rocks of the External Zones underwent accretion and fragmentation above, with a thick plastic tectonic mélange unit of a highly deformed rock assemblage, the so-called Subbetic Chaotic Complex (Vera and Martín-Algarra, 2004) where carbonates frequently constitute isolated ranges deformed by fold-and-thrusts (Crespo-Blanc and Campos 2001; Frizon de Lamotte et al., 1991; Pedrera et al., 2012).

The Estepa range is one of these isolated ranges, composed of several carbonate outcrops: the Becerrero, Hacho, Mingo, Águilas, and Pleites hill (Fig. 1b). The sedimentary sequence starts in a thick mélange unit with a matrix formed mainly by Triassic Keuper clays and evaporites (Pedrera et al., 2012; Ruiz-Constán et al., 2012). Detached above this unit, lies a Mesozoic-Palaeogene sequence. This starts with 20 to 50 m of dolomitic breccias. Over these lie 200 to 300 m of Middle Jurassic limestones (Molina, 1987). A unit of argillaceous nodular limestones was deposited above during the Middle Jurassic to Early Cretaceous. On the top, Cretaceous to Palaeocene marls and marly limestone are heterogeneously distributed with large thickness changes and sedimentary gaps (Castro and Ruiz-Ortiz, 1991). A unit of white marls, calcareous sands, limestones, and white calcarenites unconformably overlie the Mesozoic-Palaeocene Subbetic rocks, which appear to belong to the Middle Miocene. Upper Tortonian marine calcarenites, sands, and marls unconformably overlie the previous units. Plio-Quaternary continental detrital sediments belonging to the piedmont, alluvial fan, and river deposits discordantly overlie the older rocks. The piedmont and alluvial fans are particularly well developed in the SE boundary of the Pleites hill.

The Jurassic limestones and dolostones of Pleites hill also constitute a small aquifer (1.5 km^2 of outcropping carbonates). Hydrodynamic and hydrochemical studies indicate that the Pleites aquifer has a behaviour independent of the nearby aquifers that occupy the Estepa Range: the Mingo, Hacho, Águilas, and Becerrero aquifers (Martos-Rosillo et al., 2009). All its boundaries are closed to the groundwater flow, except the south-eastern border, which is partially covered by permeable Pliocene and Quaternary detrital sediments. Pumping tests enabled the calculation of a transmissivity of 2000-2500 m^2/day in the aquifer. In addition, a well storage effect was detected during the pumping tests, which was probably related to the presence of karstic cavities (Martos-Rosillo, 2008). The recharge occurs by rain water infiltration (0.38 hm^3/year, 35% of the average annual rainfall). The sharp topography of the Pleites Hill (29% of average slope gradient) leads to a lower infiltration coefficient than in the nearby aquifers. The infiltration is concentrated mainly in the south-eastern hillside, where the water flows along the epikarst and infiltrates the hillside toe. The water discharge of the Pleites aquifer occurs along the south-eastern border towards a wetland sector, which is dry at present as a consequence of the intensive exploitation of the aquifer. This setting provokes a fast drop in their water table with the frequent desiccation of the discharge zone, and deterioration in the water quality. Therefore, the freshwater is mixed with the salt water from the Triassic evaporites of the basal mélange unit, inducing an increase in the water's electric conductivity, from 450 μS/cm to 1700-2000 μS/cm.

The carbonates present an early state of karstification characterized by the development of karrens, limestone pavements, and few dolines. At the top of the hills an epikarst is developed. The thickness of the epikarst increases in the sector with a low slope, as occurs at the top of Becerrero hill. Along the south-eastern border of Pleites hill, some karstification features have been recognized (Martos-Rosillo et al., 2013). The most prominent karstic forms are dolines developed after the collapse of the carbonate and Pliocene to Quaternary alluvial sedimentary rocks (Cruz-Sanjulian, 1977). There, two water-supply boreholes, the Algaidilla I and III, perforated a buried cave between 26 and 66 m and between 49 and 66 m depth respectively, the so-called Algaidilla cave (Fig. 1).

3. Methods

The deeply buried Algaidilla cave was studied combining microgravity, ERT, and IP techniques.

3.1. Survey stations

The precise determination of the coordinates of each geophysical site is decisive for proper accurate geophysical data acquisition, processing, modeling and interpretation. The precise altitude determination is especially important in microgravity surveys, where a miscalculation of ± 1 m induces a deviation of up to ±0.2 mGal. Therefore, we attempted to make a precise determination of the altitude at each site. To do so, we used two combined microtopography techniques:

- Differential GPS. A fixed GPS reference station, consisting of a Leica 1200 GPS receiver, GPS antenna and one-watt radio transmitter was established on a point with coordinates determined respect to the Andalusian Positioning Network known as RAP (Red Andaluza de Posicionamiento, http://www.juntadeandalucia.es; http://rap.uca.es/). The Leica 1200 GPS system uses error-correction data to fine-tune the position accuracy of each geophysical site to ±0.5-20 mm. This system provides local-area error corrections for the satellite signals.
- A laser level SP30 and LC-2 laser receptor were used for high-precision determination of the relative altitude of the geophysical sites using reference points of known coordinates. The altitude accuracy of each point was to ±0.17 mm.

3.2. Microgravity

Microgravity enables the detection of near-surface bodies of small dimensions with a different density than that of their surroundings. The presence of caves constitutes a reduction in the density (0 g/cm^3 above and roughly 1 g/cm^3 below the water table) with respect to the host rock, and, therefore, in the gravity value. The negative gravity anomaly (McGrath et al., 2002) could be quantitatively modeled to determine the cave geometry.

We used an Autograv Scintrex CG-5 gravity meter with an accuracy of 0.001 mGal. The 305 gravimetric measurement stations were referred to the Granada gravimetric base (Instituto Geográfico Nacional, www.ign.es). The profile has a length of 200 m formed by measurement sites spaced 2.5 and 5 m (Fig. 2). Three profiles had a N-S orientation (profiles 1, 2 and 3) and one had an E-W orientation (profile 4) (Fig. 2). In addition, 19 additional gravity stations were measured around these profiles to draw the Bouguer anomaly map. After tidal and instrumental drift corrections, the Bouguer anomaly was determined using a reference density of 2.67 g/cm^3 and applying the terrain correction by the method of Hammer's circles (Hammer 1939, 1982). This correction was calculated from the digital terrain model of Andalusia (Junta de Andalucía, 2005) with a resolution of 10 m up to 4469 m around each measurement station (Zones B to I). The residual gravity anomaly was calculated from the Bouguer anomaly by trend removal, and also the regional anomaly determined on the basis of the 1:1,000,000 regional Bouguer anomaly maps (I.G.N., 1975).

Finally, the residual anomalies determined were forward modeled along profiles using 2.5D approximation (from 20 to 30 m orthogonal lengths) using GRAVMAG V.1.7 from the British Geological Survey (Pedley et al., 1993). Forward microgravity modeling is rather limited if the geometry of the modeled object is not partially known beforehand. Therefore, field geological and borehole data, as well as morphologies defined in the 2D resistivity inversion models, were considered during gravity forward modeling.

3.3. Electrical resistivity tomography (ERT) and induced polarization (IP)

ERT and IP methods are electrical geophysical techniques that provide detailed information of the subsurface resistivity and induced polarization distribution. ERT method consists on a lineal electrode array, where an electrical current is consecutively injected through a source electrodes pair and the potential difference is recorded between other electrode pairs. The apparent resistivity (φ_a) is determined by the ratio of the potential (V) and the current intensity (I) multiplied by a geometric factor (k) ($\varphi_a = (V/I)\cdot k$). The apparent resistivity can be equal to the effective resistivity in homogeneous and isotopic mediums. Each measurement of apparent resistivity is represented on a pseudo-section. Resistivity is sensitive to small changes in rock porosity, interconnectivity, and water salinity (Worthington, 1976).

IP method measures chargeability by the voltage decay over a specified time interval after the removal of the artificial current. The voltage does not return to zero instantaneously and decays slowly, indicating that charge has been stored in the rocks. This charge accumulates mainly at interfaces between clay minerals and around metallic conductors, which induce dielectric polarization of the ionic charges present in an aqueous medium.

We used the ABEM Terrameter SAS 4000, an electrode selector ES10-64C, 4 Lund automatic cables with 21 takeouts on each, 81 steel electrode and 12V DC battery, which constitutes a high-resolution electric imaging system. It consists of a multielectrode arrangement simultaneously used to determine both horizontal and vertical resistivity and chargeability variations along a profile (ABEM, 2006). The equipment has a resolution of 25 mV (theoretical, 1 second integration time), three automatic measurement ranges (± 250 mV, ± 10 V and ± 400 V) and an accuracy of 1% at all temperatures.

3.3.1. Forward Modeling

Using a priori information from the two existing boreholes, we constructed 2D forward models, using RES2DMOD software (Loke, 2002), with simplified geometries to examine the expected range of resistivity and chargeability contrasts in different settings. This program calculates the apparent resistivity pseudosection for a defined 2D synthetic model. The apparent resistivity pseudosections were inverted using RES2DINV software. ERT and IP forward model inversion was performed using the finite difference method based on field measurements (Dey and Morrison, 1979; Loke, 1994). Forward modeling calculation allows us to select the optimum electrode array configuration by checking the resolution, penetration and geometry of the derived anomalies (e.g. Gómez-Ortiz, 2012). The best results for our study area were obtained using a Wenner-Schlumberger array with an electrode spacing of 5 m.

3.3.2. Field acquisition

Four profiles were acquired using a 4-channel multiple gradient electrode array and two combined protocols (GRAD4LX8 and GRAD4S8; ABEM 2006) which use the Wenner-Schlumberger electrode array configuration previously tested in the forward models. The gradient array is developed for multi-channel resistivity meter system (Dahlin and Zhou, 2006). A multi-channel system can make several measurements simultaneously with the same position of the current electrodes and different localization of the potential electrode pairs. GRAD4S8 was designed to supplement GRAD4LX8 at the shortest electrode spacing. Electrodes were deployed at a 5 m and 2.5 m spacing, with effective penetration depths of ~70 and ~35 m, respectively. In addition, we combined different total lengths of profiles, between 400 and 500 m. Along profile 2, which was placed in a central position (Fig. 2), two different electrode spacings (5 m and 2.5 m) were combined, including common points, with the aim of reaching maximum penetration and a good near-surface resolution. Iterative 2D inversion of the data was performed using the smoothness-constrained least-square method (deGroot-Hedlin and Constable, 1990; Sasaki, 1992; Loke et al., 2003). The inversion process tries to reduce the RMS (root-mean-squared) value after each iteration in an attempt to find a better model. We used a mesh made up of model cells increasing in size at greater depth, using 2 nodes per unit electrode spacing and an initial damping factor of 0.3.

3.3.3. Normalized Depth of Investigation index (DOI)

The empirical depth of investigation (DOI) index method was introduced by Oldenburg and Li (1999) and modified by Marescot et al. (2003). To determine the DOI it is necessary to carry out, at least, two inversions of the data using different resistivity backgrounds. The second reference model should be obtained from an initial resistivity background 10 to 100 times higher than the first one (Loke, 2012). The equation below makes it possible to calculate a DOI index (R) of the model cell by cell:

$$R_{1,2}(x,z) = \frac{m_1(x,z) - m_2(x,z)}{m_{1r} - m_{2r}} \tag{1}$$

Where m_{1r} and m_{2r} are the resistivity of the first and second reference models, and m_1 (x, z) and m_2 (x, z) are the resistivity of each cell of these models. The DOI index (R) will approach zero where the two inversions produce the same resistivity values, regardless of the value of the reference model. In cells where the value is far from zero, it means that the resistivity value depends on the background resistivity value assigned to the reference model; such a result is not reliable. The normalized DOI index is calculated to reduce the effect of the damping factor and the selection of the initial reference model (Robert et al., 2011). To normalize the DOI index, we use the maximum value of R (R_{max}) calculated with Eq. (1):

$$R(x,z) = \frac{m_1(x,z) - m_2(x,z)}{R_{max}\ (m_{1r} - m_{2r})} \qquad (2)$$

The main difficulty lies in deciding the cut-off value where the inversion values are trusted. For the normalized DOI index, Marescot et al. (2003) recommended a cut-off value of 0.1 or 0.2. In our case, we used a more restrictive 0.1 cut-off value. We carried out two inversions with a background resistivity of the second reference model that was 100 times the first one. The computation of the normalized DOI index was performed with RES2DINV v.3.59, and it is shown on the ERT and IP profile (e.g. Robert et al., 2011).

4. Results

4.1. Microgravity results

4.1.1. Bouguer Anomaly

We calculated the Bouguer anomaly map of the study sector from 305 new microgravity measurement stations (Fig. 3). The sector had a surface area of 40,000 m^2 and a maximum height difference of 31 m from the lowest point (385 m.a.s.l.) to the highest (416 m.a.s.l.). The variation of the Bouguer anomaly is -94.274 mGal to -93.239 mGal, a range of 1.04 mGal.

The highest Bouguer anomaly value coincided with the highest sector, where the Jurassic carbonate rocks are located. The anomaly value decreased progressively towards the east in the area with a lowest topography, where low-density Quaternary alluvial rocks crop out. Superimposed over this general trend were low-amplitude negative Bouguer anomalies presumably associated with buried caves. At the top of the mountain (340.60 to 340.66 km E and 4124.125 km N), a gravity minimum is ranged between -93.5 and -93.7 mGal. The most prominent low-amplitude Bouguer anomaly minimum (-93.8 mGal) had a N-S elongated shape coinciding with the position of the buried cave of Algaidilla, in the central part of the map (340.66 to 340.70 km E; 4124.12 to 4124.18 km latitude N). The Bouguer anomaly resolution slightly decreases toward the boundaries.

4.1.2. Microgravity models

The N-S trending microgravity profiles (profile 1, 2, and 3) revealed an asymmetric minimum residual anomaly slightly displaced towards the N associated with Algaidilla cave. This minimum reached -0.45 mGal in the profile 1, -0.4 mGal in the profile 2, and -0.5 mGal in the profile 3. In the E-W oriented profile 4, the minimum caused by the cave was masked by lithological changes. Nevertheless, there were two minima, at meter 0 and at meter 20, which could be related to buried caves (Fig. 4).

We modeled the Pliocene to Quaternary alluvial detrital sediments with densities of 2.2-2.3 g/cm^3. This formation, located in the shallowest part of profiles 1 and 2, progressively decreases in thickness towards the W until completely disappearing in profile 3. These Pliocene to Quaternary alluvial sediments unconformably overlie Jurassic limestones and dolostones with density 2.55 and 2.7 g/cm^3, respectively. These carbonate rocks, with an average thickness of 60 m in the profiles modeled, enclose Algaidilla cave. The cave is located near the contact with the mélange unit having a matrix composed mainly of Triassic clay and evaporites.

Algaidilla cave is partially submerged below the water table. During the data collection, the water table is located at 345 m.a.s.l in the Algaidilla I and III boreholes. We assigned 1.02 g/cm^3 density to the water according to it salinity and temperature. To model Algaidilla cave, we used different orthogonal lengths according the plan view of the Bouguer anomaly minimum associated with the cave. The boundaries of Algaidilla cave modeled in each profile fit the results of the 2D inversion models of the electrical resistivity tomography and the available borehole data. The cave had an approximately horizontal N-S elongated morphology with a maximum length of 150 m and a width of 40 m along the E-W direction. The maximum vertical thickness located in the central zone was 25 m.

4.1.3. Electrical Resistivity Tomography and Induced Polarization

This section presents the forward modeling and measured profiles in the study area. Moreover, we describe the results of the forward modeling as well as the ERT and IP models with the trusted zone determined by calculating the DOI index.

4.1.3.1 Forward Modeling profiles

The forward modeling profiles are shown in Figure 5, and Figure 5a illustrates the influence of the steel pipes installed in the two boreholes. We assigned a resistivity of 1 ohm.m to the steel tubes and a background resistivity of 200 ohm.m linked to limestones. The model shows a conductive anomaly coinciding with the borehole position and a higher resistivity anomaly between the boreholes in the shallowest zone. These anomalies disappear at depth, where the value of the background is homogeneous. In a second setting (Fig. 5b) we performed an ERT forward modeling considering both the cave and the steel pipes. In the ERT forward model, the simplified geometry of the cave was constructed in two separate parts: a saturated cave with 0.001 ohm.m (measured water conductivity of 1171 µS/cm), and an unsaturated cave with very high resistivity, considering a value of 1000 ohm.m. Although the obtained ERT forward model of Figure 5b presents the same conductive effect in the shallowest part linked to the steel pipes, it delineates the geometry of the cave with remarkable resolution. Therefore, we discern the transition from high resistivity values (unsaturated cave) to low resistivity values (saturated cave). The IP model with decalcification clays (Fig. 5c) located high values of chargeability above the modeled body.

4.1.3.2 ERT and IP models

Resistivity models resulting from 2D numerical inversions are displayed in Figure 6. The models for profiles 1, 2, and the eastern part of profile 4 show a relatively low resistive surface layer (~50 to 75 ohm·m), corresponding to the Pliocene-Quaternary detrital sediments. A resistive zone (~857 ohm·m) extends downwards from the surface and from the lower boundary of the low resistive surface layer in all the 2D resistivity models, coinciding with the Jurassic limestones and dolostones (Fig. 6). The resistive values are abruptly distorted by vertical lower resistivity bodies, which match with the location of the Algaidilla I and III steel-cased boreholes. The Algaidilla I borehole (390 m.a.s.l) cut the cave between 26 and 66 m (between 364 and 328 m.a.s.l.) and the Algaidilla III borehole (388 m.a.s.l.) between 49 and 66 m (between 339 and 322 m.a.s.l.). The boreholes are placed closely to meters 0 and 40 in the N-S oriented profiles (profiles 1, 2 and 3) and to the meter 0 in profile 4 (vertical dashed black lines in Fig. 6). The intersection of the boreholes with the cave coincides with an intermediate to low resistivity feature with a boundary that approximately matches the 250 ohm·m resistivity contour line. These intermediate resistivity values are presumably associated with the presence of moderately saline groundwater in the cave. The morphology of the resistivity anomaly has been used to constraint the models of the microgravimetry data. The models show a low resistive zone towards the base, potentially indicating the location of the mélange unit, with a matrix composed mainly of Triassic clay and evaporites, beneath the Jurassic carbonates.

The IP models resulting from 2D numerical inversions show a high chargeability body partially coinciding with the location of Algaidilla cave (profiles 1, 2 and 3 in Fig. 6). We interpreted these chargeability values as clays derived from the dissolution of carbonate rocks that must be deposited at the bottom of the cave.

The incidence of the cave in the E-W oriented profile 4 is unclear, apparently due to its limited depth resolution. The resistivity value coinciding with the top of the cave, according to the borehole Algaidilla I, matches with the background resistivity assigned to the limestones and dolostones. The IP model reveals a high chargeability sector at the base of the model towards the E (Profile 4, Fig. 6) which could belong to the Triassic Keuper clay-in-matrix mélange.

We computed the depth of investigation for surveyed data, based on the DOI index method, following the recommendations given by Oldenburg and Li (1999) and Marescot et al. (2003). The 0.1 cut-off value of the DOI index obtained is highlighted on the profiles with a continuous white line (Fig. 6). The zones above the line marked, which have a DOI value between 0 and 0.1, show an overall high resolution. Underneath the line, where the DOI index begins to point towards high values, it indicates the untrusted zones of the profile. Note that reliable zones delimited by the DOI index of the models extend to a depth of 70 ~ 80 m in the middle sectors. This is greater than the depth of the bottom of the cave, as derived from the resistivity models.

5. Tentative 3D model

From the combined electric tomography, microgravimetry, and borehole data, we constructed an approximate 3D model of Algaidilla cave (Fig. 7). For this, the cave’s boundaries were defined in each interpreted section (rounded dashed black lines in Figure 6). The sections interpreted were integrated with the topography and water table altitude data. We used Geomodeller software, which employs potential fields to build a 3D surface (Aug et al., 2005) from the sections interpreted.

Based on the geophysical models, Algaidilla cave has N-S trending tubular morphology being narrower in its southern part and progressively widening towards the north. The cavity should be roughly horizontal in the central and northern regions, whereas in the southern part the cave slopes towards the south. The estimated volume of the cavity is of ~150000 m^3, of which 78000 m^3 belong to the unsaturated zone and 72000 m^3 to the volume of water contained in the cave.

6. Discussion

Electrical tomography has been successfully used to find cavities at more than 20 m in depth (Shi et al. 1997; El-Qady, 2005; Noel and Xu 1992; Manzanilla et al. 1994; Kaufmann et al., 2011). However, in the case of caves located in carbonate rocks, due to the resistive character of the host rock (1000-100,000 ohm.m, Palacky, 1987), detection depends on the size and depth of the cave and its content (air and/or water). On the other hand, the caves have an associated minimum gravity residual anomaly that can be modeled quantitatively (Al-Rawi and Rezkalla, 1987). The present study provides information on the sensitivity of electrical tomography and microgravity prospecting to detect partially flooded caves located more than 30 m below the ground surface.

6.1. Methodological implications

The high resolution achieved with Bouguer anomaly data (305 microgravity stations) allowed the qualitative identification of anomaly minima that could potentially be produced by karst cavities. Therefore, Algaidilla cave, which was highlighted by borehole data, gave a -0.5 mGal residual gravity minimum. Thus, these results validate the approach of using a high-resolution Bouguer anomaly map as a preliminary step to the qualitative identification of buried caves and the selection of sectors most of interest to be investigated in detail using other geophysical methods.

However, when quantitative microgravimetric direct modeling is used alone, it fails because unlimited models are able to adjust the data of gravity residual anomaly. In our case, borehole data and 2D ERT and IP results were used together for better constraint of the possible models. It is well known the non-uniqueness and instability of ERT inverse solution and the diverse anomaly shapes resulting from different selected electrode arrays. We have checked the resolution of different electrode arrays and compared the resulting images from various configurations. Although the iterative inversion process minimizes this non-linear problem, the ratio layer thickness and layer conductivity could be solved with multiple solutions due to principle of equivalence. In our example the boundaries of the cave are constrained by boreholes partially resolving the void thickness. Thus, the value of 250 ohm·m was used to delineate the contours of top of Algaidilla cave in 2D resistivity inversion models 1, 2 and 3 (corresponding to profiles of the same name). The 2D resistivity inversion model 4 did not detect the cave because the profile of the cavity runs parallel to the hillside slope and the abrupt topography limits the penetration. Although steel tubes of two boreholes affect the shallow part of the ERT models, as in the forward models, the geometry of the cave is well resolved by the tomography data and it can delineated at a depth between 26 and 66 m. In addition, the obtained DOI guarantees reliable results in the ERT and IP models with 0.1 cut-off values down to 70 - 80 m or beneath, which is greater than the depth of the cave bottom.

There was a difference in the resistivity values associated with the cave between profile 1 and profile 3. The profile 1 showed a progressive change from higher resistivity values in the upper part of the cave to lower values towards the base. In profile 3 the maximum value of resistivity coincided with the central part of the cave. This discrepancy between the values of resistivity profiles potentially indicates that the section below the water table is larger than the unsaturated zone in profile 1. In this setting, the moderately saline water filling the bottom of the cave produces low resistivity values. However, in profile 3, most of the cavity remains above the unsaturated zone, which is reflected in the high resistivity values. Our results suggest that in karstified carbonate massifs, cavities lying below the water table have a larger resistivity contrast with the resistive host bedrock than above the water table. However deepest sectors of the models should be interpreted with caution since they are less constrained by the data.

IP models show areas with high polarization values located mainly at the bottom of the cave. Although, the deepest parts of the models are less constrained, these chargeability positive anomalies are probably associated to decalcification clays generated from the dissolution of the calcite from the rock. Therefore, these red decalcification clays were cross-cut by the Algaidilla I and III boreholes. A decalcification clays residuum commonly occurs in karstic caves. Calcite dissolves in water saturated in carbonic anhydride and the impurities, red clays with iron oxide, precipitates. These clays are transported by the water and deposited in the base of the cavity. IP is observed when a steady current through two electrodes is shut off and the voltage does not return to zero instantaneously, indicating that charge has been stored mainly at interfaces between clay minerals. This study illustrates the strong potential of the IP method to highlight decalcification clays and therefore to complement other geophysical techniques during cave detection.

While caves commonly have a highly resistive electrical signature (e.g. El-Qady et al., 2005; Gambetta et al., 2011), our study reveals that caves that develop below the water table have lower resistivity than do the surrounding carbonates. Therefore, while Algaidilla cave has sharp resistivity contrast in the saturated part, the resistivity contrast is lower above the water table.

This study demonstrates the reliability of ERT and IP, combined with gravity prospecting, for deep and saturated cave detection, compared with the GPR method. On the one hand, GPR penetrates up to 15 m, but it fails in high-conductivity materials such as water or saturated clays. Thus, while it is a suitable method for detecting shallow unsaturated caves, the low penetration below the water table rules out its use for deep saturated caves. Moreover, in this setting, we have demonstrated the sensitivity of IP prospecting to detect the clays that are commonly associated with the carbonate dissolution in karstic caves.

6.2. Cave development, hydrogeological and engineering implications

The geophysical results show that Algaidilla cave developed from karstification along a N-S direction coinciding with the boundary strike between dolostones and the mélange unit, which is saturated in saline water. The mélange unit acts as an aquitard saturated in highly saline water. At present, the conductivity values measured show moderate salinity. The intensive exploitation of the Pleites carbonate aquifer would lead to the mixture between deeper saline waters and the shallow freshwater. This would result in deteriorated water quality that could limit its use for irrigation.

The location and geometry of Algaidilla cave estimated from geophysical modeling serve as a warning against nearby overexploitation, to prevent cave-in situations. Collapsed caves have been described along the eastern hillside of the Pleites hill (Cruz-Sanjulian, 1977), close to and with an equivalent setting as the cave studied. Therefore, load-addition by the construction of buildings or roads with heavy vehicular traffic could cause Algaidilla cave to collapse. At present, there is a minor country road with very little road traffic above the cave. Increasing the traffic or passing with heavy machinery could cause minor destabilization which, in the future, could result in a collapse.

7. Conclusions

The combined application of microgravity and electrical tomography, including resistivity (ERT) and induced polarization (IP) techniques, yields important information about the location and geometry of karstic caves deeply buried in carbonates. Algaidilla cave, which is partially saturated, has a -0.5 mGal residual gravity anomaly minimum. ERT results delineate the cavity both above and below the water table. The cave is identified as a feature having intermediate to low resistivity, its top boundary approximately matching the 250 ohm·m in the 2D ERT inversion model. The saturated part of the cave, below the water table, has lower resistivity than the surrounded carbonates, contrary to the commonly found highly resistive electrical signature of the caves. In addition, IP models show high chargeability anomalies probably associated with decalcification clays accumulated at the base of the cave. Both electrical and microgravity models reveal a cave between 20 and 66 m depth with an approximately horizontal N-S elongated shape with a maximum length of 150 m and a width of 40 m. The obtained Normalized Depth of Investigation index (DOI) —considering a cut-off value of 0.1— guarantees reliable results in the ERT and IP models down to 70 m ~ 80 m, which is greater than the depth of the base of the cave. In this setting, microgravity may constitute a preliminary regional reconnaissance method while ERT and IP results roughly constrain the geometry of the void, although it is necessary to combine them to gain accurate results for deep caves.

Acknowledgements

We are sincerely grateful to D. Francisco Jose Cabello, who facilitated the field work. We appreciate the thoughtful comments and suggestion made by Dr. Teresa Teixidó, Dr. José Peña and the support of Dr. M. H. Loke. We thank two anonymous reviewers for their insightful reviews which significantly helped to improve the manuscript. This research was supported by the CSD2006-00041, CGL-2008-03474-E/BTE, CGL2010-21048, P09-RNM-5388 and RNM148 projects.

References

ABEM, 2006. Instruction Manual Terrameter SAS 4000 / SAS 1000. ABEM Instrument AB, Sundbyberg, Sweden. 136 pp.

Abu-Shariah, M.I.I., 2009. Determination of cave geometry by using a geoelectrical resistivity inverse model. Engineering Geology 105, 239–244.

Al-Rawi, F.R., Rezkalla, J.S., 1987. The application of microgravity survey for cave detection in a karstic area. Large rock caverns. Proceedings of the international symposium, Helsinki, Finland, 2, 25-28.

Aug, C., Chilès, J.P., Courrioux, G., Lajaunie, C., 2005. 3D Geological Modelling and Uncertainty: The Potential-field Method. Quantitative Geology and Geostatistics 14, 145–154.

Beres, M., Luetscher, M., Olivier, R., 2001. Integration of ground-penetrating radar and microgravity methods to map shallow caves. Journal of Applied Geophysics 46, 249-262.

Bozzo, E., Lombardo, S., Merlanti, F., 1996. Geophysical studies applied to near-surface karst structures: the dolines. Annali di Geofisica XXXIX (1), 23-38.

Brown, W.A., Stafford, K.W., Shaw-Faulkner, M., Grubbs, A., 2011. A comparative integrated geophysical study of Horseshoe Chimney Cave, Colorado Bend State Park, Texas. International Journal of Speleology 40 (1), 9-16.

Butler, D.K., 1984. Microgravity and gravity gradient techniques for detection of subsurface cavities. Geophysics 49 (7), 1084–1096.

Cardarelli, E., Cercato, M., Cerreto, A., Di Filippo, G., 2010. Electrical resistivity and seismic refraction tomography to detect buried Cavities. Geophysical Prospecting 58, 685-695.

Carpenter, P.J., Ekberg, D.W., 2006. Identification of buried sinkholes, fractures and soil pipes using ground-penetrating radar and 2D electrical resistivity tomography. Proceedings of the Highway Geophysics - NDE Conference, 437-449.

Castro, J.M. and Ruiz-Ortiz, P.A., 1991. Nivel condensado con estromatolitos pelágicos en el Cretácico de la Sierra de Estepa (Subbético Externo, provincia de Sevilla). Revista de la Sociedad Geológica de España 4, 305–319.

Chamon, N., Dobereiner, L., 1988. An example of the use of geophysical methods for the investigation of a cavern in sandstones. Bulletin of Engineering Geology and the Environement 38, 37-43.

Chico, J.R., 1964. Detection of Caves by Gravimetry. Speleology 1, 101-108.

Crespo-Blanc, A., Campos, J., 2001. Structure and kinematics of the South Iberian paleomargin and its relationship with the Flysch Trough units: extensional tectonics within the Gibraltar Arc fold-and-thrust belt (western Betics). Journal of Structural Geology 23, 1615-1630.

Cruz-Sanjulian, J., 1977. Formas Kársticas en materiales de pie de monte. Tecniterrae. Revista española de geología y minería 16, 1-6.

Dahlin, T., Zhou, B., 2006. Gradient array measurement for multi-channel 2D resistivity imaging. Near Surface Geophysics (4), 113-123.

Dey, A., Morrison, H. F., 2005. Resistivity modeling for arbitrarily shaped two-dimensional structures. Geophysical Prospecting 27, 1020-1036.

deGroot-Hedlin, C., Constable, S., 1990. Occam's inversion to generate smooth, twodimensional models form magnetotelluric data. Geophysics, 55, 1613-1624.

El-Qady, G., Hafez, M., Abdalla, M.A., Ushijima, K., 2005. Imaging subsurface cavities using geoelectric tomography and ground-penetrating radar. Journal of Cave and Karst Studies 67 (3), 174–181.

Frizon de Lamotte, D., Andrieux, J., Guezou, J.C., 1991. Cinématique des chevauchements néogènes dans l'Arc bético-rifain: discussion sur les modèles géodynamiques. Bulletin de la Société Géologique de France 162 (4), 611–626.

Gambetta, M., Armadillo, E., Carmisciano, C., Stefanelli, P., Cocchi, L., Tontini, F.C., 2011. Determining geophysical properties of a nearsurface cave through integrated microgravity vertical gradient and electrical resistivity tomography measurements. Journal of Cave and Karst Studies 73 (1), 11–15.

García-Hernández, M., López-Garrido, A.C., Rivas, P., Sanz de Galdeano, C., Vera, J.A., 1980. Mesozoic paleogeographic evolution of the External Zones of the Betic Cordillera. Geology Mijnb., 59, 155-168.

Gibson, P.J., Lyle, P., George, D.M., 2004. Application of resistivity and magnetometry geophysical techniques for near-surface investigations in karstic terranes in Ireland. Journal of Cave and Karst Studies 66 (2), 35-38.

Gómez-Ortiz, D., Martín-Crespo, T., 2012. Assessing the risk of subsidence of a sinkhole collapse using ground penetrating radar and electrical resistivity tomography. Engineering Geology 149-150, 1-12.

Guérin, R., Baltassat J.M., Boucher, M., Chalikakis, K., Galibert P.Y., Girard J.F., Plagnes, V., Valois, R., 2009. Geophysical characterisation of karstic networks. Application to the Ouysse system (Poumeyssen, France). Comptes Rendus Geoscience 341, 810-817.

Hammer, S., 1939. Terrain corrections for Gravimeters Stations. Geophysics 4, 184-194.

Hammer, S., 1982. Critique of Terrain Corrections for Gravity Stations. Geophysics 47, 839-840.

I.G.N., 1975. Mapa de España de Anomalía de Bouguer. I.G.N., Madrid (Scale 1:1000000).

Junta de Andalucía, 2005. Digital Terrain Model of Andalusia. DVD.

Junta de Andalucía, 2011. Andalusian Positioning Network (RAP). http://www.juntadeandalucia.es/obraspublicasytransportes/redandaluzadeposicionamiento/rap/

Kaufmann, G., Romanov, D., Nielbock R., 2011. Cave detection using multiple geophysical methods: Unicorn cave, Harz Mountains, Germany. Geophysics 76, B71.

Lange A.L., 1999. Geophysical studies at Kartchner Caverns State Park, Arizona. Journal of Cave and Karst Studies 61(2), 68–72.

Lazzari, M., Loperte, A., Perrone, A., 2010. Near surface geophysics techniques and geomorphological approach to reconstruct the hazard cave map in historical and urban areas. Advances in Geosciences 24, 35-44. www.adv-geosci.net/24/35/2010/.

Leucci, G., 2006. Contribution of Ground Penetrating Radar and Electrical Resistivity Tomography to identify the cavity and fractures under the main Church in Botrugno (Lecce, Italy). Journal of Archaeological Science 33, 1194–1204.

Leucci, G., De Giorgi, L., 2005. Integrated geophysical surveys to assess the structural conditions of a karstic cave of archaeological importance. Natural Hazards and Earth System Sciences 5, 17-22.

Leucci, G., De Giorgi, L., 2010. Microgravity and ground penetrating radar geophysical methods to map the shallow karstic cavities network in a coastal area (Marina Di Capilungo, Lecce, Italy). Exploration Geophysics 41, 178-188.

Loke, M. H., 1994. The inversion of two-dimensional resistivity data. PhD thesis, Un. Of Birmingham.

Loke, M.H., Acworth, I. and Dahlin, T., 2003. A comparison of smooth and blocky inversion methods in 2D electrical imaging surveys. Exploration Geophysics, 34, 182-187.

Loke, M. H., 2002. Rapid 2D resistivity forward modeling using the finite-difference and finite-element methods. RES2Dmod v. 3.0 software. Geotomo Software Company.

Loke, M. H., 2012. Tutorial: 2-D and 3-D electrical imaging surveys. Geotomo Software Company.

Manzanilla, L., Barba, L., Chávez, R., Tejero, A., Cifuentes, G., Peralta, N., 1994. Caves and geophysics: An approximation to the underworld of Teotihuacan, México. Archaeometry 36 (1), 141–157.

Marescot, L., Loke, M.H., Chapellier, D., Delaloye, R., Lambiel, C., Reynard, E., 2003. Assessing reliability of 2D resistivity imaging in mountain permafrost studies using the Depth Of Investigation index method. Near Surface Geophysics (1), 57-67.

Martos-Rosillo, S. 2008. Investigación hidrogeológica orientada a la gestión racional de acuíferos carbonáticos sometidos a un uso intensivo del agua subterránea. El caso de la Sierra de Estepa (Sevilla). Tesis Doctoral. Universidad de Granada, Granada.

Martos-Rosillo, S., Rodríguez-Rodríguez, M., Moral., F., Cruz-Sanjulián, J.J., and Rubio, J.C. 2009. Analysis of groundwater mining in two carbonate aquifers in Sierra de Estepa (SE Spain) based on hydrodynamic and hydrochemical data. Hydrogeology Journal 17, 1617-1627.

Martos-Rosillo, S., Rodríguez-Rodríguez, M., Pedrera, A., Cruz-San Julián, J.J., and Rubio, J.C., 2013. Quantifying the groundwater recharge in semiarid carbonate aquifers with an intensive use: The Estepa range aquifers (Seville, South of Spain). Environmental Earth Science.

McCann, D.M., Jackson, P. D., Culshaw, M.G., 1987. The use of geophysical surveying methods in the detection of natural cavities and mineschafts. Quarterly Journal of Engineering Geology 20, 59-73.

McGrath, R.J., Styles, P., Thomas, E., Neale, S., 2002. Integrated high resolution geophysical investigations as potential tools for water resource investigations in karst terrain. Environmental Geology 42, 552-557.

Mochales, T., Casas, A.M., Pueyo, E.L., Pueyo, O., Román, M.T., Pocoví, A., Soriano, M.A., Ansón, D., 2008. Detection of underground cavities by combining gravity, magnetic and ground penetrating radar survey: a case study from the Zaragoza area, NE Spain. Environmental Geology 53, 1067-1077.

Molina, J.M., 1987. Análisis de facies del Mesozoico en el Subbético Externo (provincia de Córdoba y sur de Jaen). Doctoral Thesis, University of Granada. 518 p.

Noel, M., Xu, B., 1992. Cave detection using electrical resistivity tomography. Cave Science 19, 91–94.

Oldenburg, D.W., Li, Y., 1999. Estimating depth of investigation in dc resistivity and IP surveys. Geophysics 64, 403-416.

Ortega, A.I., Benito-Calvo, A., Porres, J., Pérez-González, A., Martín Merino, M.A., 2010. Applying Electrical Resistivity Tomography to the Identification of Endokarstic Geometries in the Pleistocene Sites of the Sierra Atapuerca (Burgos, Spain). Archaeological Prospection 17, 233-245.

Owen, T.E. 1983. Detection and mapping of tunnels and caves. In: Fitch, A.A. (ed.) Developments in Geophysical Exploration Methods 5, 161–258.

Palacky, G.J. 1987. Resistivity characteristics of geological targets. In: Electromagnetic Methods in Applied Geophysics - Theory, Vol. 1., Investigations in geophysics Series, Volume 3 (E.B. Neitzel Ed.). USA, 53-129.

Pánek, T., Margielewski, W., Táborík, P., Urban, J., Hradecký, J., Szura, C., 2010. Gravitationally induced caves and other discontinuities detected by 2D electrical resistivity tomography: Case studies from the Polish Flysch Carpathians. Geomorphology 123, 165-180.

Pedley, R.C., Busby, J.P. y Dabeck, Z.K., 1993. GRAVMAG User Manual - Interactive 2.5D gravity and magnetic modelling. British Geological Survey, Technical Report, WK/93/26/R.

Pedrera, A., Marín-Lechado, C., Martos-Rosillo, S., Roldán, F. J., 2012. Curved fold-and-thrust accretion during the extrusion of a synorogenic viscous allochthonous sheet: The Estepa Range (External Zones, Western Betic Cordillera, Spain). Tectonics, Vol. 31.

Rădulescu, V., Rădulescu, F., Diacopolos, C., Popescu, M., 2007. Geoelectrical Study for Delineating Underground Cavities in Karst Areas. GEO-ECO-MARINA 13, 89-95.

Ravbar, N., Kovačič, G., 2010. Characterisation of karst areas using multiple geo-science techniques, a case study from SW Slovenia. Acta Carsologica 39 (1), 51–60.

Robert, T, Dassargues, A, Brouyère, S, Kaufmann, O, Hallet, V, & Nguyen, F., 2011. Assessing the contribution of electrical resistivity tomography (ERT) and self-potential (SP) methods for a water well drilling program in fractured/karstified limestones. Journal of Applied Geophysics, 75 (1), 42-53.

Rodríguez Castillo, R., Reyes Gutierrez, R., 1992. Resistivity identification of shallow mining cavities in Real del Monte, México. Engineering Geology 33, 141-149.

Ruiz-Constán, A., Pedrera, A., Galindo-Zaldívar, J., Pous, J., Arzate, J., Roldán-García, F.J., Marín-Lechado, C., Anahnah, F., 2012. Constraints on the frontal crustal structure of a continental collision from an integrated geophysical research: The central-western Betic Cordillera (SW Spain). Geochemistry Geophysics Geosystem, Vol. 13 (8).

Sasaki, Y., 1992. Resolution of resistivity tomography inferred from numerical simulation. Geophysical Prospecting 40, 453-464.

Shi, W., Morgan, F.D. & Wharton, A.E., 1997. Application of electrical resistivity tomography to image Harrison Caves in Barbados, West Indies. Society of Exploration Geophysicists 67th Annual Meeting: Expanded Abstracts 1, 350–353.

Smith, D.L., Randazzo, A.F., 1975. Detection of Subsurface Solution Cavities in Florida Using Electrical Resistivity Measurements. Southeastern Geology 16 (4), 227-240.

Valois, R., Bermejo, L., Guérin, R., Hinguant, S., Pigeaud, R., Rodet, J., 2010. Karstic morphologies identified with geophysics around Saulges caves (Mayenne, France). Archaeological Prospection 17, 151–160.

Vargemezis, G., Tsourlos, P., Papazachos, C., Kostopoulos, D., 2007. Application of electrical resistivity tomography to the detection of the Ermakia (Northern Greece) cavity system. Bulletin of the Geological Society of Greece XXXX. Proceedings of the 11th International Congress, Athens, 2007.

Vera, J. A., Martín-Algarra, A., 2004. Cordillera Bética y Baleares. In: Geología de España (J. A. Vera Ed.).

Worthington, P. F. (1976), Hydrogeophysical Equivalence of Water Salinity, Porosity and Matrix Conduction in Arenaceous Aquifers. Ground Water, 14, 224–232.

Zhou, Q.Y., Matsui, H., Shimada, J., 2004. Characterization of the unsaturated zone around a cavity in fractured rocks using electrical resistivity tomography. Journal of hydraulic research 42, 25-31.

Figure captions

Figure 1. (a) Synthetic geological map of the Gibraltar Arc, formed by the Betic and Rif Cordilleras. (b) Geological map of the Estepa Range. The locations of geological cross-section of Figure 1c and Figure 2 are marked. (c) Geological cross-section of the Estepa Range, note that the Pleites hill corresponds to a SE-vergent fold above a thrust. (Modified of Pedrera et al., 2012)

Figure 2. Aerial photography of the study sector with the location of the geophysical sites.

Figure 3. Bouguer anomaly map plotted above the digital elevation model. The gravity sites are marked as black dots.

Figure 4. 2D forward models constructed from the residual gravity anomalies.

Figure 5. Forward modeling of ERT profiles including synthetic models and inverted pseudosections. (a) Resistivity profile with two boreholes embedded in a homogeneous half-space, (b) resistivity profiles with a partially saturated cave located between the two boreholes and (c) induced polarization profile of decalcification clays associated at the base of the cave.

Figure 6. Inversion models of electrical resistivity and induced polarization tomography. RMS error and number of iterations are marked. The cave contour is marked with a black dashed line and the water table (WT) is indicated with a white dashed line. The DOI index 0.1 cut-off value is marked on each profile.

Figure 7. Three-dimensional construction of the Algaidilla cave from the geophysical results found using a 3D potential field (Aug et al., 2005).

Table caption

Table 1. Studies using gravity and/or electrical methods, and their combination with other geophysical techniques used for detecting caves. The approximate penetration depth is also indicated. Electrical methods: IP - Induced Polarization tomography; ERT

– 2D Electrical resistivity tomography; VES – Vertical electrical Soundings. Electromagnetic methods: EM – Electromagnetic; GPR – Ground Penetration Radar; NP – Natural Potential. Magnetic methods: M – Magnetometry; MRS – Magnetic Resonance Sounding. Gravity methods: G – Gravimetry. Seismic methods: SRT – Seismic Refraction tomography.

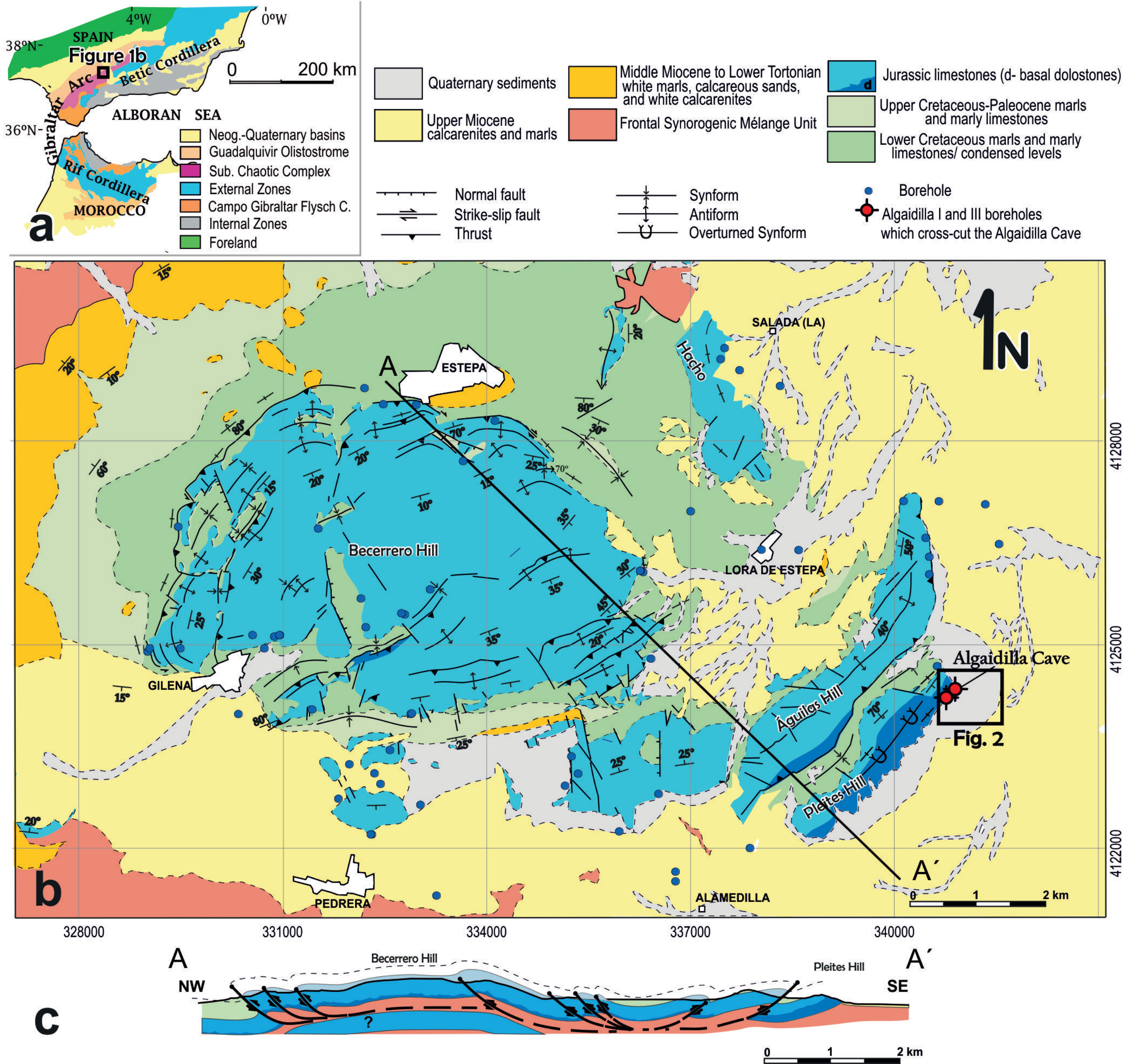

a
4ºW
0ºW
38ºN
36ºN
SPAIN
Figure 1b
Betic Cordillera
Arc
Gibraltar
ALBORAN SEA
Rif Cordillera
MOROCCO
0
200 km
Neog.-Quaternary basins
Guadalquivir Olistostrome
Sub. Chaotic Complex
External Zones
Campo Gibraltar Flysch C.
Internal Zones
Foreland
Quaternary sediments
Upper Miocene calcarenites and marls
Middle Miocene to Lower Tortonian white marls, calcareous sands, and white calcarenites
Frontal Synorogenic Mélange Unit
Jurassic limestones (d- basal dolostones)
d
Upper Cretaceous-Paleocene marls and marly limestones
Lower Cretaceous marls and marly limestones/ condensed levels
Normal fault
Strike-slip fault
Thrust
Synform
Antiform
Overturned Synform
Borehole
Algaidilla I and III boreholes which cross-cut the Algaidilla Cave
b
N
A
A´
ESTEPA
SALADA (LA)
Hacho
Becerrero Hill
LORA DE ESTEPA
GILENA
Águilas Hill
Pleites Hill
Algaidilla Cave
Fig. 2
PEDRERA
ALAMEDILLA
0
1
2 km
328000
331000
334000
337000
340000
4128000
4125000
4122000
c
A
A´
NW
SE
Becerrero Hill
Pleites Hill
?
0
1
2 km

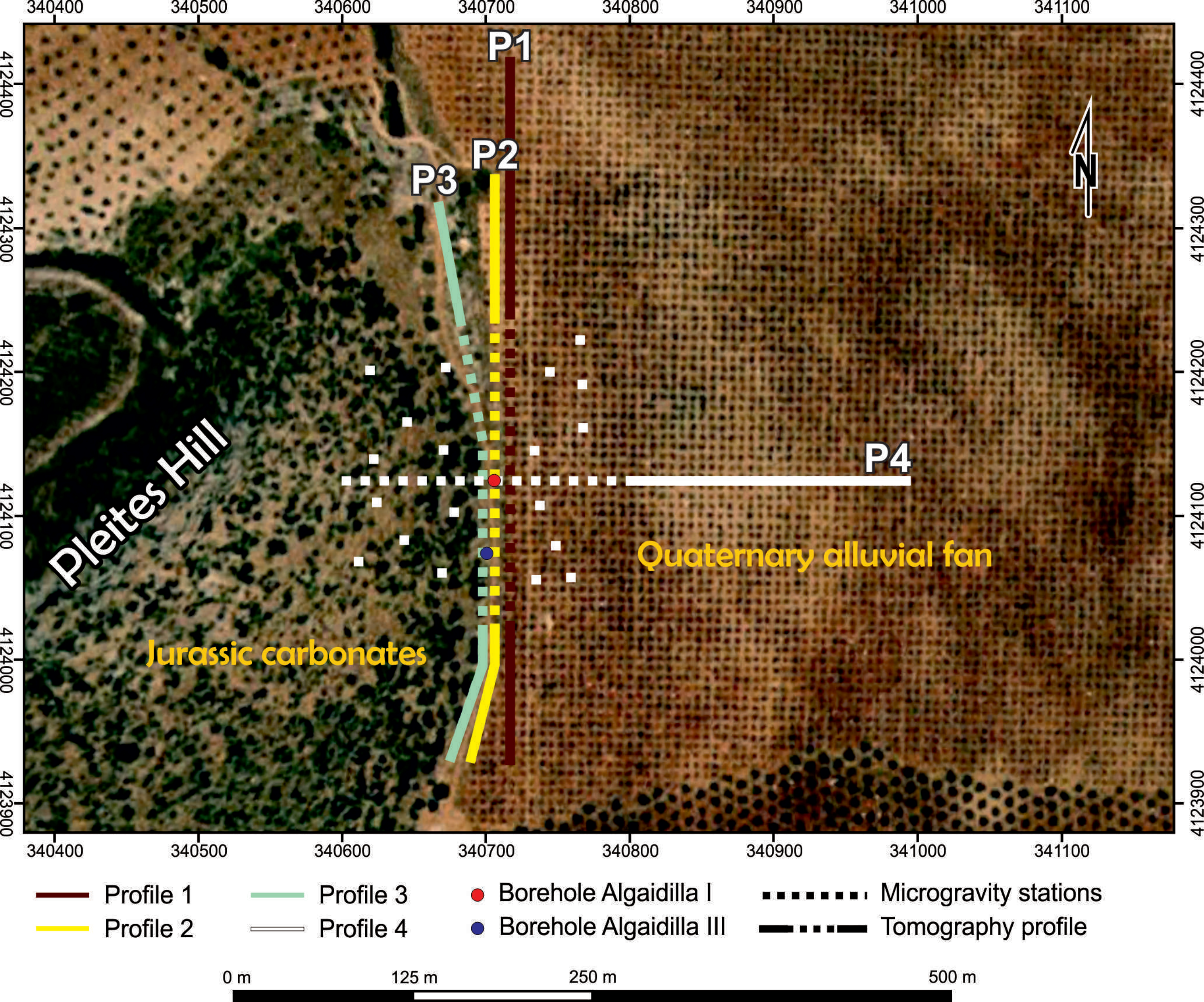
340400
340500
340600
340700
340800
340900
341000
341100
4124400
4124300
4124200
4124100
4124000
4123900
P1
P2
P3
P4
N
Pleites Hill
Quaternary alluvial fan
Jurassic carbonates
Profile 1
Profile 2
Profile 3
Profile 4
Borehole Algaidilla I
Borehole Algaidilla III
Microgravity stations
Tomography profile
0 m
125 m
250 m
500 m

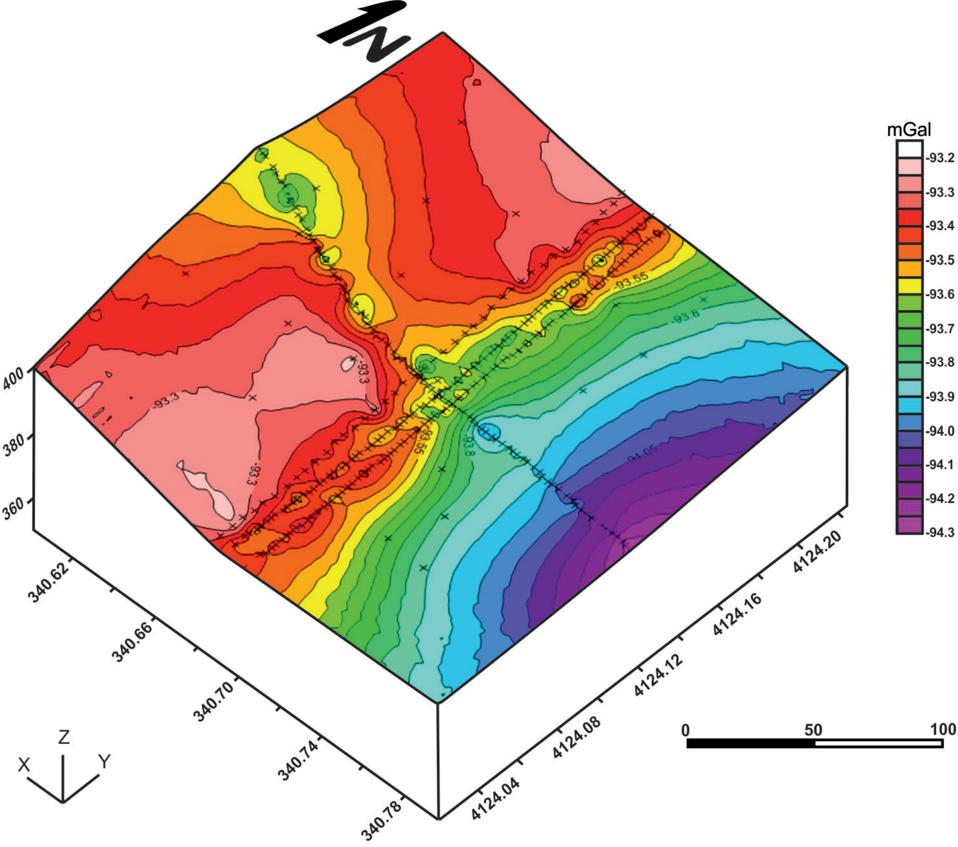
N
mGal
-93.2
-93.3
-93.4
-93.5
-93.6
-93.7
-93.8
-93.9
-94.0
-94.1
-94.2
-94.3
-93.3
-93.3
-93.3
-93.55
-93.55
-93.8
-93.8
-94.05
400
380
360
340.62
340.66
340.70
340.74
340.78
4124.04
4124.08
4124.12
4124.16
4124.20
0
50
100
Z
X
Y

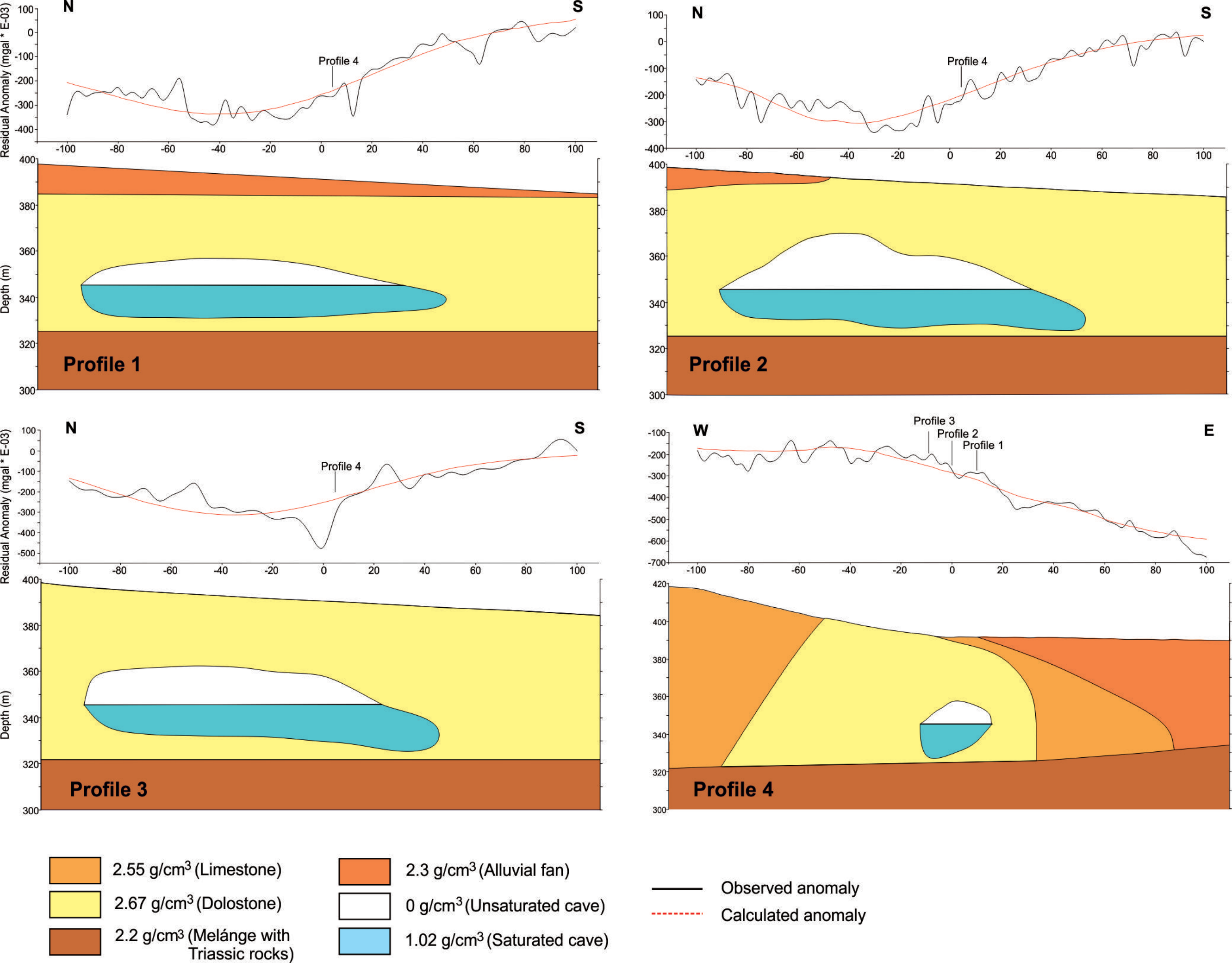
N
S
Residual Anomaly (mgal * E-03)
Depth (m)
Profile 4
Profile 1
Profile 2
Profile 3
Profile 3
Profile 2
Profile 1
W
E
Profile 4
100
0
-100
-200
-300
-400
-500
-600
-700
-100
-80
-60
-40
-20
0
20
40
60
80
100
420
400
380
360
340
320
300
2.55 g/cm3 (Limestone)
2.67 g/cm3 (Dolostone)
2.2 g/cm3 (Melánge with Triassic rocks)
2.3 g/cm3 (Alluvial fan)
0 g/cm3 (Unsaturated cave)
1.02 g/cm3 (Saturated cave)
Observed anomaly
Calculated anomaly

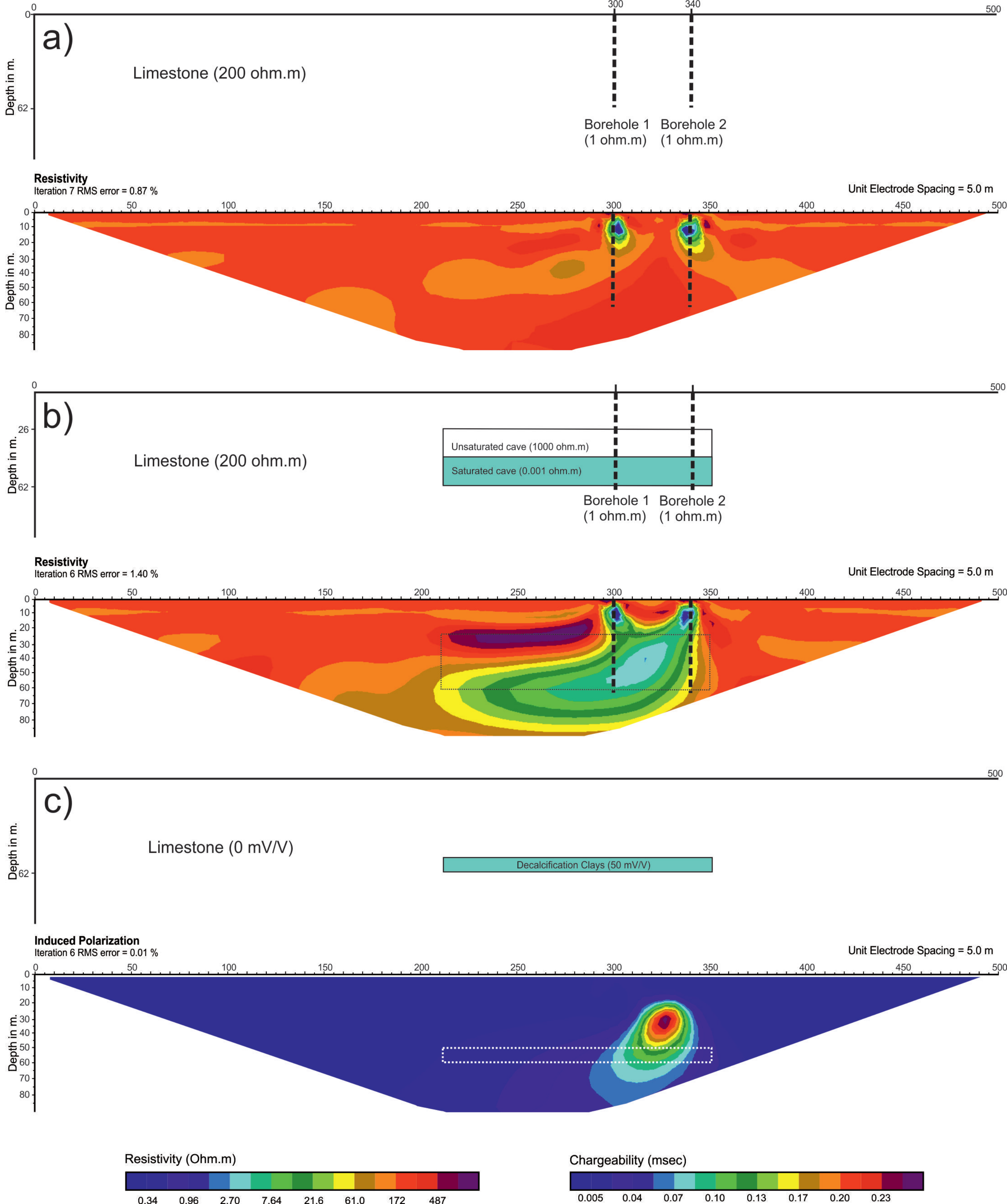
a)
Limestone (200 ohm.m)
Borehole 1 (1 ohm.m)
Borehole 2 (1 ohm.m)
Depth in m.
0
62
300
340
500
Resistivity
Iteration 7 RMS error = 0.87 %
Unit Electrode Spacing = 5.0 m
b)
Limestone (200 ohm.m)
Unsaturated cave (1000 ohm.m)
Saturated cave (0.001 ohm.m)
Borehole 1 (1 ohm.m)
Borehole 2 (1 ohm.m)
26
62
Resistivity
Iteration 6 RMS error = 1.40 %
Unit Electrode Spacing = 5.0 m
c)
Limestone (0 mV/V)
Decalcification Clays (50 mV/V)
Induced Polarization
Iteration 6 RMS error = 0.01 %
Unit Electrode Spacing = 5.0 m
0 50 100 150 200 250 300 350 400 450 500
0 10 20 30 40 50 60 70 80
Resistivity (Ohm.m)
0.34 0.96 2.70 7.64 21.6 61.0 172 487
Chargeability (msec)
0.005 0.04 0.07 0.10 0.13 0.17 0.20 0.23

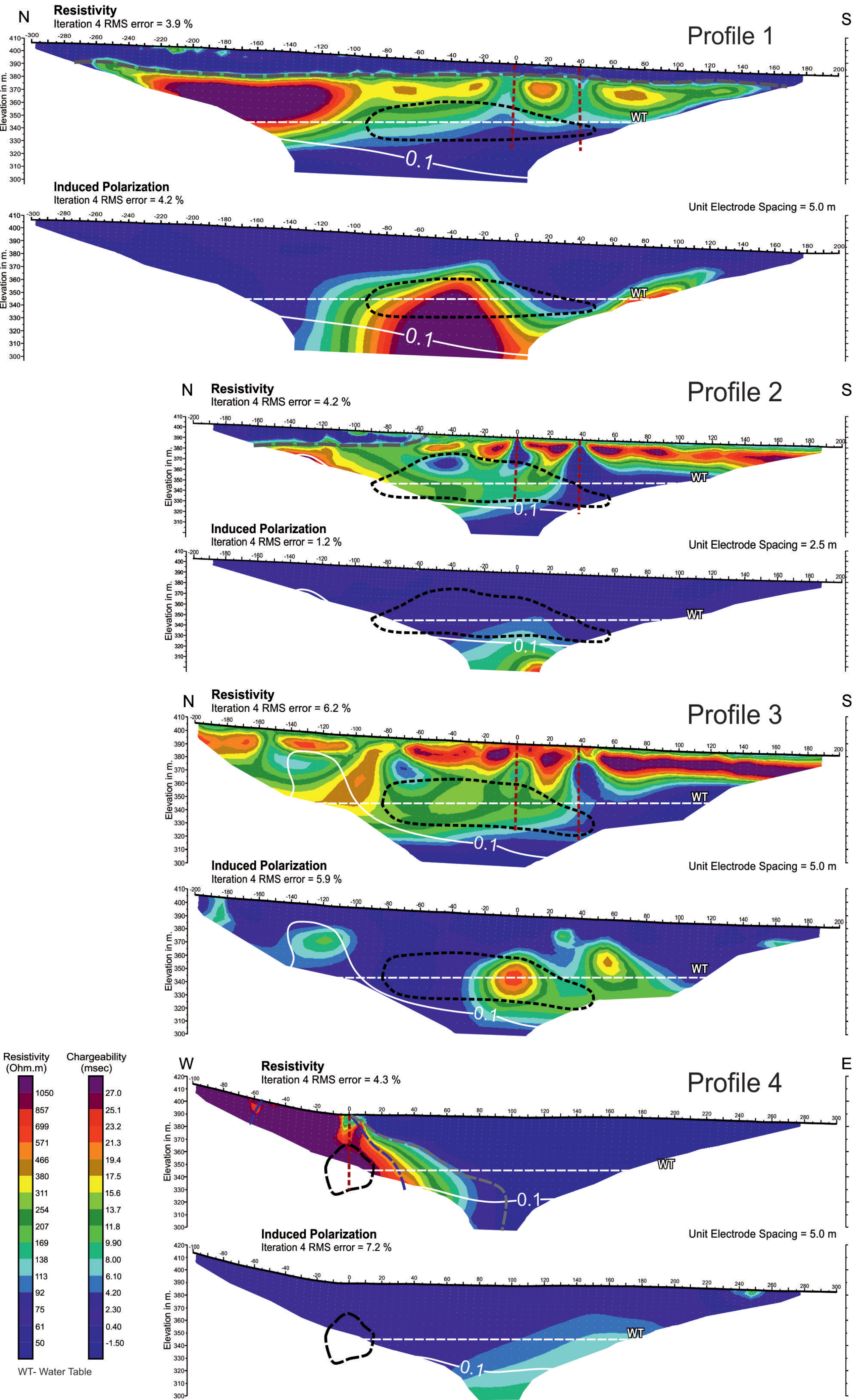
N
Resistivity
Iteration 4 RMS error = 3.9 %
Profile 1
S
Elevation in m.
WT
0.1
Induced Polarization
Iteration 4 RMS error = 4.2 %
Unit Electrode Spacing = 5.0 m
N
Resistivity
Iteration 4 RMS error = 4.2 %
Profile 2
S
Induced Polarization
Iteration 4 RMS error = 1.2 %
Unit Electrode Spacing = 2.5 m
N
Resistivity
Iteration 4 RMS error = 6.2 %
Profile 3
S
Induced Polarization
Iteration 4 RMS error = 5.9 %
Unit Electrode Spacing = 5.0 m
W
Resistivity
Iteration 4 RMS error = 4.3 %
Profile 4
E
Induced Polarization
Iteration 4 RMS error = 7.2 %
Unit Electrode Spacing = 5.0 m
Resistivity (Ohm.m)
1050
857
699
571
466
380
311
254
207
169
138
113
92
75
61
50
Chargeability (msec)
27.0
25.1
23.2
21.3
19.4
17.5
15.6
13.7
11.8
9.90
8.00
6.10
4.20
2.30
0.40
-1.50
WT- Water Table

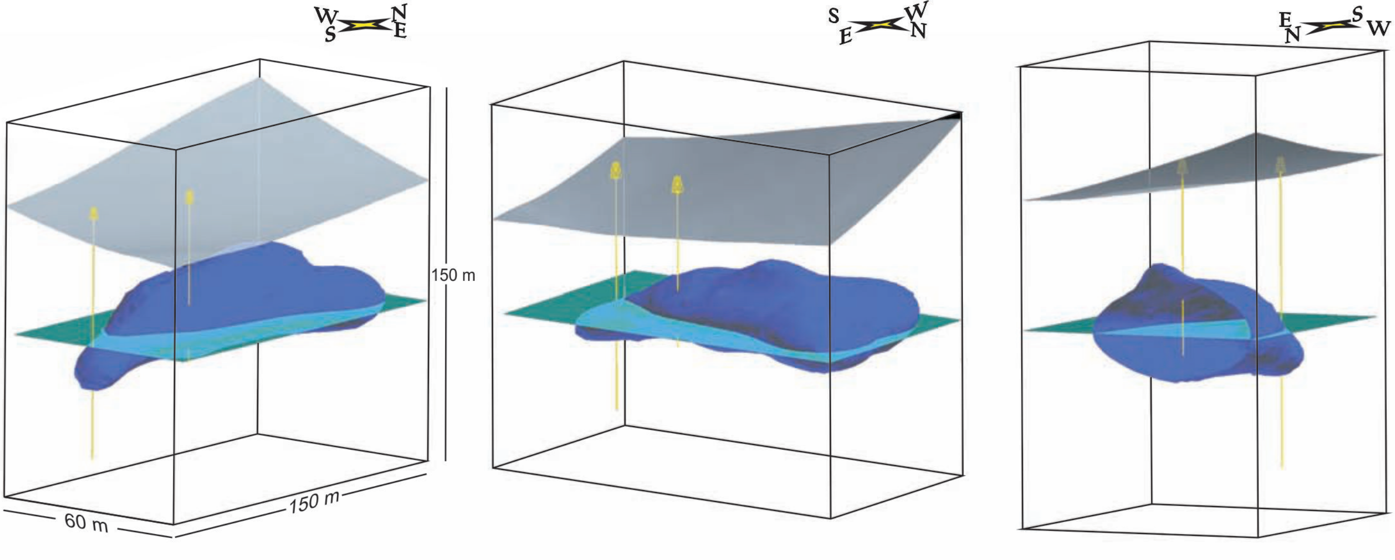
W
N
S
E
150 m
60 m
150 m
S
W
E
N
E
S
N
W

Author, year	*Methods	Depth (meters)
Leucci and Giorgi, 2005	GPR and ERT	4
Zhou et al., 2004	ERT	4
Leucci and Giorgi, 2010	GPR and MG	5
Brown et al, 2011	MG, GPR, ERT, IP	10
El Qady et al., 2005	GPR and ERT	10
McGrath et al., 2002	G and ERT	10
Ortega et al, 2010	ERT	12
Beres et al., 2001	MG and GPR	14
Leucci, 2006	GPR and ERT	15
Vargemezis et al., 2007	ERT	15
Abu-Shariah, 2009	ERT	16
McCann et al., 1987	SRT and Seismic Resonance, Cross-hole, ERT, G, M and EM	16
Smith and Randazzo, 1975	VES	16
Carpenter and Ekberg, 2006	GPR and ERT	19
Bozzo et al., 1996	EM, ERT, SRT	20
Lazzari et al., 2010	GPR and ERT	20
Ravbar and Kovačič, 2009	ERT	20
Cardarelli et al., 2010	ERT and SRT	25
Mochales et al., 2008	G, M and GPR	28
Butler, 1984	G and G gradient	30
Gambetta et al., 2011	G and ERT	30
Santos and Afonso, 2005	ERT	30
Valois et al., 2010	ERT and SRT	30
Guérin et al., 2009	ERT, MRS, “mise-à-la-masse” electrical mapping and SRT.	40
Pánek et al, 2010	ERT	40
Rodríguez and Reyes, 1992	VES	40
Gibson et al., 2004	ERT and M	44
Chamon and Dobereiner, 1988	ERT, M, G and EM	50
Lange, 1999	EM, G and NP	80
Rădulescu et al., 2007	ERT and VES	80